The Sommerfeld ground-wave limit for a molecule adsorbed at a surface

Li Chen [2*]†‡, Jascha A. Lau[1,2]‡, Dirk Schwarzer[2], Jörg Meyer[3], Varun B. Verma[4], Alec M. Wodtke[1,2,5]

[1]Institute for Physical Chemistry, University of Göttingen, Tammannstr. 6, 37077 Göttingen, Germany

[2]Department of Dynamics at Surfaces, Max-Planck Institute for Biophysical Chemistry, Am Faßberg 11, 37077 Göttingen, Germany

[3]Leiden Institute of Chemistry, Gorlaeus Laboratories, Leiden University, P.O. Box 9502, 2300 RA Leiden, The Netherlands

[4]National Institute of Standards and Technology, Boulder, Colorado, USA

[5]International Center for Advanced Studies of Energy Conversion, Georg-August University of Göttingen, Tammannstraße 6, 37077 Göttingen, Germany

† Present address: State Key Laboratory of Molecular Reaction Dynamics, Dalian Institute of Chemical Physics, Chinese Academy of Sciences, Dalian, Liaoning 116023, People's Republic of China

‡These authors contributed equally to this work

[*]Correspondence to: alec.wodtke@mpibpc.mpg.de & li.chen@mpibpc.mpg.de

Abstract

Using a mid-infrared emission spectrometer based on a superconducting nanowire single-photon detector (SNSPD), we observe the dynamics of vibrational energy pooling of CO adsorbed at the surface of a NaCl crystal. After exciting a majority of the CO molecules to their first vibrationally excited state (v=1), we observe infrared emission from states up to v=27. Kinetic Monte Carlo simulations show that vibrational energy collects in a few CO molecules at the expense of those up to eight lattice sites away by selective excitation of NaCl's transverse phonons. The vibrating CO molecules behave like classical oscillating dipoles, losing their energy to NaCl lattice-vibrations via the electromagnetic near-field. This is analogous to Sommerfeld's description of the Earth's influence on radio transmission by ground waves.

Main Text

Polar molecules in optical lattices formed by interfering laser beams are platforms for studying quantum magnetism (*1*), quantum many-body dynamics (*2*) and quantum computing (*3, 4*). The electric fields at a crystalline surface are another form of lattice, one capable of orienting and ordering polar molecules. Hence, adsorbing molecules to low-temperature solids might be a complementary and, so far, unexplored approach to studying the lattice dynamics of polar molecules. Unfortunately, dynamical interactions between adsorbates and solid substrates are

typically much stronger than those between adsorbed molecules (*5, 6*). For example, an adsorbate's vibrational energy may flow to a solid's electrons within picoseconds (*7, 8*) or, due to intrinsically anharmonic interatomic forces, to lattice vibrations within nanoseconds (*9, 10*).

One exception is a monolayer of CO adsorbed to NaCl (100) – see Fig. 1c. Here, dipole-dipole interactions between CO molecules are stronger than CO-NaCl interactions, conditions that lead to vibrational energy pooling (VEP). Chang et al. observed VEP producing CO in states at least up to v=15 by near-resonant vibration-to-vibration (V-V) energy transfer.

$$\begin{array}{ll} CO(1) + CO(1) \rightarrow CO(2) + CO(0) & + \Delta\varepsilon(2) \\ CO(2) + CO(1) \rightarrow CO(3) + CO(0) & + \Delta\varepsilon(3) \\ \vdots & \vdots \\ CO(v) + CO(1) \rightarrow CO(v+1) + CO(0) & + \Delta\varepsilon(v+1) \end{array} \qquad (1)$$

Unfortunately, detailed studies were impossible due to the low sensitivity and poor time-response of infrared detectors available at that time (*11*).

In this work, we detect time- and wavelength-resolved laser-induced infrared fluorescence with a superconducting nanowire single-photon detector (SNSPD) (*12, 13*) in order to study VEP in detail. Kinetic Monte Carlo (kMC) simulations (*14-18*) of our observations reveal V-V energy transfer occurring between CO molecules separated by more than eight lattice sites and show that the excess energy represented by $\Delta\varepsilon(v+1)$ in Eq. (1) is selectively absorbed by NaCl's transverse phonons. Surprisingly, the vibrating CO molecules behave like classical oscillating dipoles, losing their energy to NaCl lattice-vibrations via the electromagnetic near-field. These rates are quantitatively described by a theory (*19, 20*) that has its origins in Sommerfeld's 1909 description of a radio transmitter interacting with the Earth forming damped electromagnetic surface waves (*21*). This is a weak coupling limit where the anharmonic interatomic forces normally so important to energy flow can be completely neglected.

Figures 1A & B show infrared spectra of CO adsorbed to NaCl obtained in absorption (panel A) and with laser-induced infrared fluorescence (panel B). The spectrum of the CO monolayer is composed of a doublet centered at 2052 cm^{-1}, where the intensity pattern is polarization sensitive. The feature at 2055 cm^{-1} results from the symmetric stretching of the two coupled CO molecules in the 2×1 unit cell (shown as a dashed rectangle in panel C) (*22, 23*). The 2049 cm^{-1} line observed with s- and p-polarization arises from the anti-symmetric stretch vibration. For comparison, panel B shows the laser-induced infrared fluorescence excitation spectrum obtained from a CO monolayer for both p- and s- polarization. There can be no doubt that the laser-induced fluorescence results from the excitation of CO molecules in the monolayer.

Figure 2A & B show the experimentally obtained fluorescence emission spectrum (in black) compared to kMC simulations (in red). All features in these spectra result from the first overtone emission of vibrationally excited CO; the emitting vibrational state is indicated by combs. Intensity peaks reflecting enhanced vibrational populations are seen near v=7, 16 and 25; hereafter, we refer to vibrational states near these three values of v as base-camp 1, 2, and 3, respectively.

The red curve in Fig. 2A shows a kMC simulation under our experimental conditions where only nearest neighbor V-V energy transfer is permitted, an assumption used in previous work (*14-18*).

This approach yields a peak in population at v~8 (base-camp 1), strongly resembling Fig. 3 of Ref.'s (*14*) and (*15*) but markedly different than experiment. Note that a single molecule with only 4 nearest neighbors can still reach v=8 since the nearest neighbors can transport vibrational quanta from more distant molecules by process (2).

$$\mathrm{CO}(1) + \mathrm{CO}(0) \rightarrow \mathrm{CO}(0) + \mathrm{CO}(1) \qquad \Delta\varepsilon(1) = 0 \qquad (2)$$

Population in states higher than v~8 is prevented by a one-phonon energy cut-off (*14, 15*) that is reached when $\Delta\varepsilon(v+1)$ – see Eq. (1) – exceeds the energy of the highest frequency phonon of the NaCl substrate. Clearly, the nearest neighbor assumption in these kMC simulations fails to describe the experiment.

To produce molecules in higher vibrational states, long distance interactions between vibrationally excited molecules are needed. When vibrational energy pooling is modelled including V-V exchange over an area of ~1000 Å^2, kMC simulations reproduce experiment well (Fig. 2B, red curve). In this case, vibrationally excited molecules in base-camp 1 states can interact with one another even though they are not likely to be nearest neighbors. For example, processes like

$$\begin{gathered} \mathrm{CO}(7) + \mathrm{CO}(7) \rightarrow \mathrm{CO}(8) + \mathrm{CO}(6) \\ \mathrm{CO}(8) + \mathrm{CO}(7) \rightarrow \mathrm{CO}(9) + \mathrm{CO}(6) \\ \vdots \\ \mathrm{CO}(v) + \mathrm{CO}(7) \rightarrow \mathrm{CO}(v+1) + \mathrm{CO}(6) \end{gathered} \qquad (3)$$

allow molecules in base-camp 1 states to climb to base-camp 2, where again the one-phonon energy cut-off slows further pooling. Subsequently, molecules in base-camp 2 climb to base-camp 3 by even longer range interactions. Vibrational states higher than v=27 are not seen as energy transfer to the lowest lying excited electronic states becomes possible (V-E energy transfer). The temporal sequence of base-camp formation can also be seen by taking snap shots of the vibrational distribution in the kMC simulations at different times (see Fig. 2C). This shows that base-camp 1 forms within 100 ns, base-camp 2 within 0.1-1 μs and base-camp 3 only after 10-100 μs.

The distance dependence of dipole-dipole interactions explains the sequential formation of base-camps. From the kMC simulations of Fig. 2B, we find that the average distance between pooling molecules forming base-camp 1 is 4.1 Å (approx. 1 lattice constant); whereas, for base-camp 2 this distance is 11.7 Å and for base-camp 3 it is 17.6 Å. One-phonon-assisted V-V rates scale with distance as R^{-8} – see supplementary material – meaning base-camp 1 is formed 10^3 times faster than base-camp 2 which is formed 10^2 times faster than base-camp 3. This hierarchy of rates is consistent with our experimental observations.

VEP selectively excites transverse NaCl phonons. Figure 3 (left panel) shows four kMC simulations (red, blue, green & brown) of emission spectra using different assumptions about the solid's phonon density of states and compares them to experiment (black). (The assumed phonon density of states used in each simulation appears in the right panel.) While all four simulations resemble experiment, we find best agreement with experiment when only transverse phonons are allowed to accept energy in the ladder climbing process. In fact, only here do we see the formation of three base-camps.

Under conditions of this work, VEP rapidly produces CO in many vibrationally excited states. Relaxation of the system back to vibrational equilibrium proceeds more slowly – see Fig. 4A where we show measurements of the time-resolved infrared fluorescence (open symbols) from seven vibrational states. Asymptotically, they all exhibit exponential decay (solid lines) with effective lifetimes, shown as open circles with error bars in Fig. 4B. For kMC simulations of the asymptotic exponential fall-off, we include three elementary processes: V-V energy transfer between CO molecules,

$$CO(v') + CO(v'') \rightarrow CO(v' + 1) + CO(v'' - 1) \tag{4}$$

spontaneous radiative emission,

$$CO(v') \rightarrow CO(v'-1) + h\nu_{IR} \tag{5}$$

and vibrational energy transfer to the NaCl lattice vibrations.

$$CO(v') \rightarrow CO(v'-1) + \Delta E_{phonon} \tag{6}$$

For process (4) we use the same approach that allowed successful simulation of the data of Fig.'s 2 and 3. See Section F of the SI. For process (5), we use the known radiative emission rate constants for gas-phase CO(v´). For process (6) we have tested two models of vibrational energy transfer. The solid squares in Fig. 4B are the effective lifetimes that result from implementation of the Skinner-Tully (ST) model described in detail in section F of the SI (*14*) – here, anharmonic coupling of CO vibration to NaCl phonons is mediated via the CO-NaCl surface bond (*14-18*). The predicted effective lifetimes are in poor agreement with experiment and they exhibit a vibrational quantum number dependence that is far too strong. (Note the logarithmic scale).

We also tested a model developed by Chance, Prock and Silbey (CPS) (*19, 20*), shown as filled circles in Fig. 4B. The CPS theory is briefly described in section F4 of the SI. The agreement with experiment is striking. CPS was developed to describe fluorescence lifetimes of dye molecules interacting through an inert spacer layer with an absorbing and reflecting solid (*24-29*). Here, coupling occurs through electromagnetic fields. The fact that CPS accurately reproduces the observations of this work, suggests that CO vibrational relaxation to NaCl lattice-vibration also occurs through the electromagnetic near-field despite the fact that there is a surface bond.

We emphasize that the weak vibrational quantum number dependence of the effective lifetime is indicative of coupling via the electromagnetic field – ST predicts a change in effective lifetime of four orders of magnitude over the same range of v where CPS predicts less than a ten-fold change. Of course, the ST model could in future be improved, an *ab initio* treatment of the coupling to the solid's phonon bath is still lacking. Despite this, we expect the strong v-dependence to be retained – see SI. Referring to Fig. 4B, we speculate that the steeper slope above v~23 indicates a transition to ST behavior.

Normally, we consider energy flow within an ensemble of oscillators to be a consequence of interatomic anharmonicity. This work shows that we can bind a molecule to a solid with sufficient strength to create samples that are stable over long periods of time without any influence of anharmonicity on the vibrational energy relaxation. In this Sommerfeld ground-wave limit, vibrational relaxation occurs exclusively via the electromagnetic field obeying the CPS model.

Here, the strength of coupling scales with the solid's imaginary index of refraction and the square of the molecule's transition dipole moment – see SI. Besides CO on NaCl, other similar systems are to be expected. CO on KCl and N_2 on NaCl are both interesting possibilities, whose CPS coupling would be even weaker than seen here. For dipolar adsorbates that find themselves within this limit, the solid's crystalline lattice can be exploited to produce spatial registry and orientational order while the strength of dipole-dipole interactions between the adsorbate molecules still far exceeds the adsorbate coupling to the solid. The prospect to study quantum lattice dynamics in systems like this appears promising.

Supplementary Content includes: 1) Materials and Methods, 2) Supplementary Text, 3) Figs. S1 to S6 and 4) References (32-48)

References and Notes

[1] J. Park *et al.*, Science **357**, 372 (2017).

[2] B. Yan *et al.*, Nature **501**, 521 (2013).

[3] D. DeMille, Phys Rev Lett **88**, 4 (2002).

[4] A. Andre *et al.*, Nat Phys **2**, 636 (2006).

[5] K. Golibrzuch *et al.*, Ann Rev Phys Chem **66**, 399 (2015).

[6] A. M. Wodtke, Chem Soc Rev **45**, 3641 (2016).

[7] J. D. Beckerle *et al.*, Phys Rev Lett **64**, 2090 (1990).

[8] P. R. Shirhatti *et al.*, Nat Chem **10**, 592 (2018).

[9] P. Guyotsionnest *et al.*, Phys Rev Lett **64**, 2156 (1990).

[10] K. Lass *et al.*, J Chem Phys **123**, 4 (2005).

[11] H. C. Chang *et al.*, Phys Rev Lett **65**, 2125 (1990).

[12] L. Chen *et al.*, Acc Chem Res **50**, 1400 (2017).

[13] L. Chen *et al.*, Optics Express **26**, 14859 (2018).

[14] S. A. Corcelli *et al.*, J Chem Phys **116**, 8079 (2002).

[15] S. A. Corcelli *et al.*, J Phys Chem A **106**, 10849 (2002).

[16] E. T. D. Boney *et al.*, J Chem Phys **139**, (2013).

[17] S. A. Corcelli, Yale University, (2002).

[18] S. A. Egorov *et al.*, J Chem Phys **103**, 1533 (1995).

[19] R. R. Chance *et al.*, Adv Chem Phys **37**, 1 (1978).

[20] R. R. Chance *et al.*, J Chem Phys **60**, 2744 (1974).

[21] A. Sommerfeld, Ann. Phys.-Leip. **28**, 665 (1909).

[22] J. Heidberg *et al.*, J Chem Phys **95**, 9408 (1991).

[23] D. Schmicker *et al.*, J Chem Phys **95**, 9412 (1991).

[24] K. H. Drexhage *et al.*, Ber Bunsenges Phys Chem **70**, 1179 (1966).

[25] K. H. Drexhage, Scientific American **222**, 108 (1970).

[26] K. H. Drexhage *et al.*, Ber Bunsenges Phys Chem **72**, 329 (1968).

[27] H. Kuhn, Naturwissenschaften **54**, 429 (1967).

[28] H. Kuhn, J Chem Phys **53**, 101 (1970).

[29] K. H. Tews *et al.*, Nature **228**, 276 (1970).

[30] H. C. Chang *et al.*, J Chem Phys **89**, 7561 (1988).

[31] J. Heidberg *et al.*, J Electron Spectrosc Relat Phenom **64-5**, 227 (1993).

[32] J. Estel *et al.*, Surf Sci **54**, 393 (1976).

[33] H. J. Chen *et al.*, Chinese Physics B **24**, (2015).

[34] J. P. Perdew *et al.*, Phys Rev Lett **77**, 3865 (1996).

[35] V. Blum *et al.*, Comput. Phys. Commun. **180**, 2175 (2009).

[36] H. J. Monkhorst *et al.*, Phys. Rev. B **13**, 5188 (1976).

[37] P. Haas *et al.*, Phys. Rev. B **79**, (2009).

[38] P. Haas *et al.*, Phys. Rev. B **79**, (2009).

[39] G. X. Zhang *et al.*, New J Phys **20**, (2018).

[40] K. Parlinski *et al.*, Phys Rev Lett **78**, 4063 (1997).

[41] A. Togo *et al.*, Scripta Materialia **108**, 1 (2015).

[42] R. R. Chance *et al.*, J Chem Phys **62**, 2245 (1975).

[43] R. R. Chance *et al.*, J Chem Phys **60**, 2184 (1974).

[44] H. Kuhn *et al.*, Angewandte Chemie-International Edition **10**, 620 (1971).

[45] A. Baños, in *International series of monographs on electromagnetic waves.* (Pergamon Press, Oxford, New York, 1966).

[46] L. E. Brus, J Chem Phys **74**, 737 (1981).

[47] A. D. Boese *et al.*, J Phys Chem C **120**, 12637 (2016).

[48] E. D. P. J. E. Eldridge, *Handbook of Optical Constants of Solids*. E. D. Palik, Ed., Sodium Chloride (NaCl) (Academic Press, New York, 1997), vol. 1.

Acknowledgements

We thank S. A. Corcelli for sharing his kinetic Monte Carlo simulation code and A. Kandratsenka for helpful discussions. We also thank Prof. Fabian Heidrich-Meisner for providing helpful suggestions after reading an early version of this manuscript. J.M. gratefully acknowledges financial support from The Netherlands Organisation for Scientific Research (NWO) under Vidi Grant No. 723.014.009.

Figures

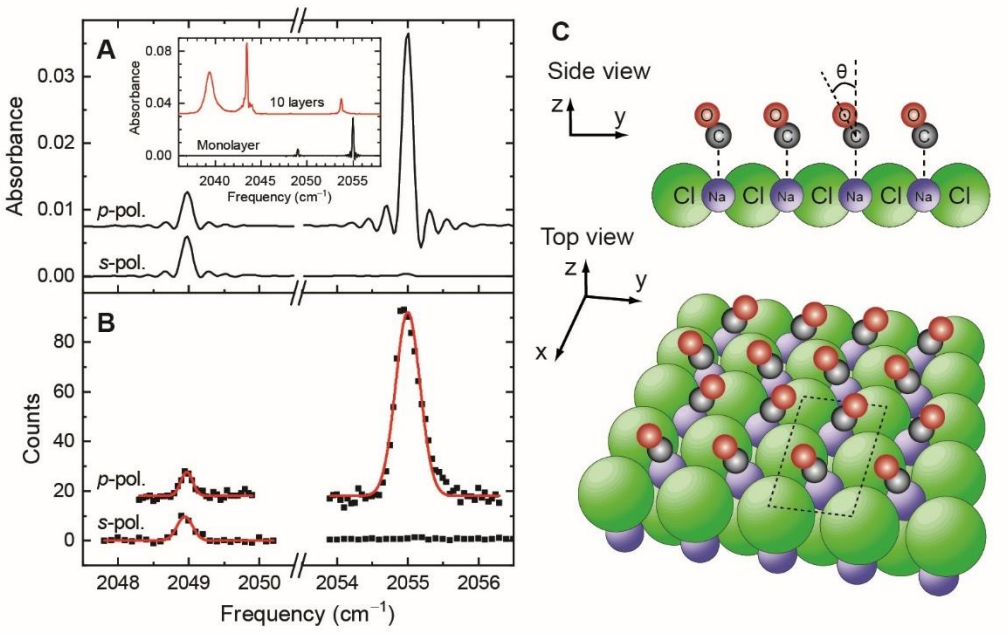

Figure 1 | Structure and infrared spectroscopy of the $^{13}C^{18}O$ monolayer on NaCl(100): The polarization dependent monolayer spectrum is observed with (A) FTIR absorbance spectroscopy and (B) laser-induced infrared fluorescence by scanning the laser excitation frequency and integrating the total fluorescence signal between 50 and 1050 μs after the laser pulse. The spectra were recorded at a surface temperature of ~ 7 K. Note that the baseline of the p-polarized spectra is shifted for clarity. The inset in panel A shows that the IR absorption spectrum of the CO monolayer (black) is clearly distinguishable from that of a multilayer (red) for p-polarized light. CO molecules in the multilayer but not in contact with the NaCl surface give rise to a doublet centered at 2042 cm^{-1} (*30*, *31*). The feature at 2054 cm^{-1} arises from the CO molecules at the buried NaCl interface (*31*). The monolayer line intensities have been corrected for an offset of 18° in the polarization of the FTIR spectrometer light source. In panel B, the experimental data is represented by square symbols and red lines are Gaussian fits to guide the eye. Panel C: Structure of the monolayer CO on NaCl(100) (*22*, *23*). The nearest neighbour CO-CO distance is 3.96 Å. At a surface temperature below 35 K, the CO molecules are tilted with respect to the surface normal by an angle of 25°, and arranged in antiparallel oriented rows to form a *p*(2×1) unit cell, as depicted by the dashed rectangle.

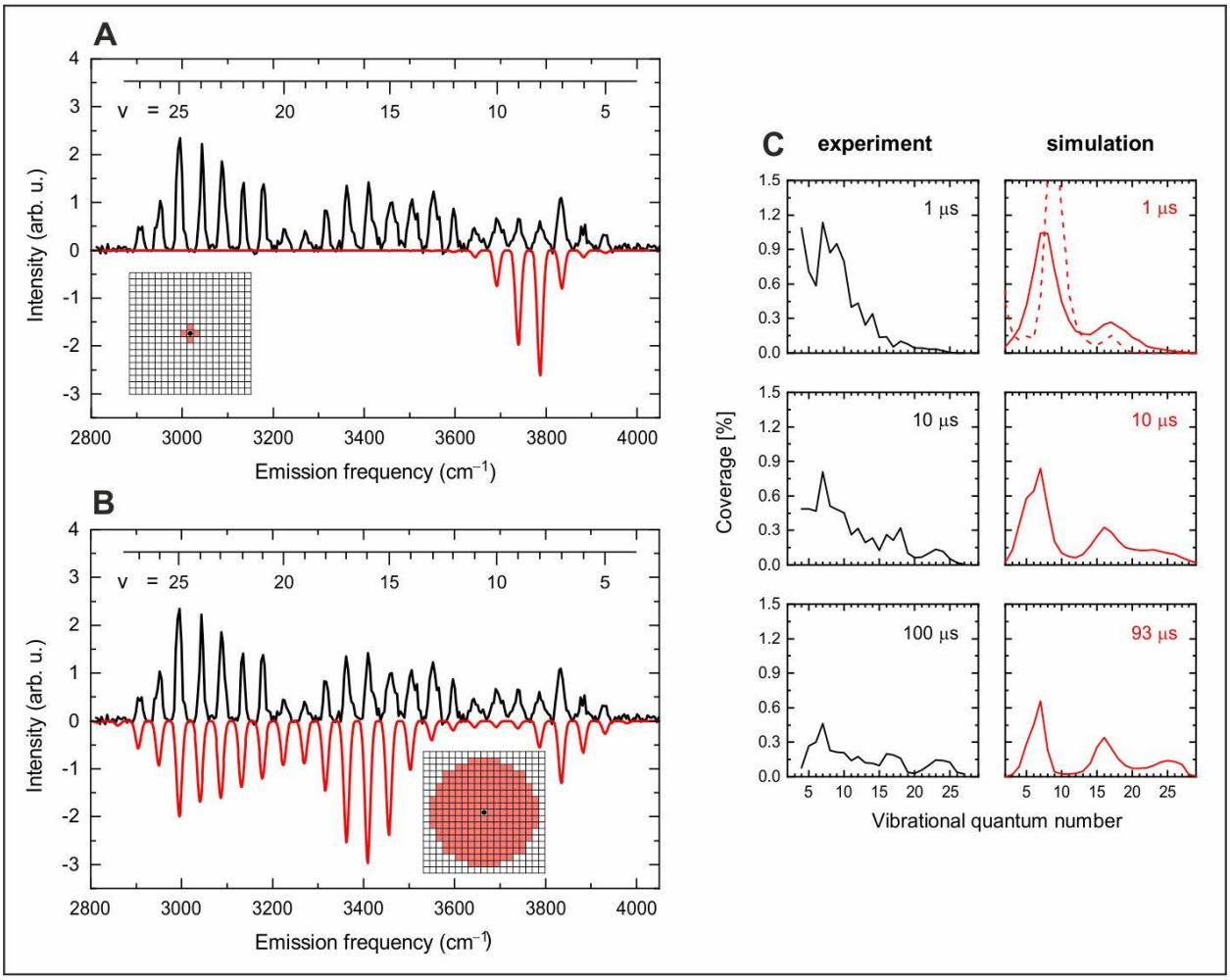

Figure 2 | Base-camp pooling mechanism operating for a monolayer of CO on NaCl(100): In panels A and B, we show the experimentally observed emission spectrum (black solid lines) and simulated spectra using kinetic Monte Carlo methods (red solid lines). The insets represent the CO lattice and the red shaded areas visualize the interaction distance around a given CO molecule (black dot) used in each kMC simulation. In panel A, the simulation allows only nearest neighbor V-V exchange, an assumption that was also made in Ref.'s (*14-16*). In panel B, the simulation includes molecular interactions out to a distance of 34 Å. In each case, the monolayer feature at 2055 cm^{-1} (Fig. 1B) was excited with a narrowband infrared laser and the emission was dispersed through a monochromator and detected with an SNSPD integrating the signal-counts between 50 and 250 µs after the laser pulse. Panel C: Snap shots in the experimentally derived and simulated population distributions showing sequential formation of the base-camps. Note that the red dashed line corresponds to the population distribution at 100 ns.

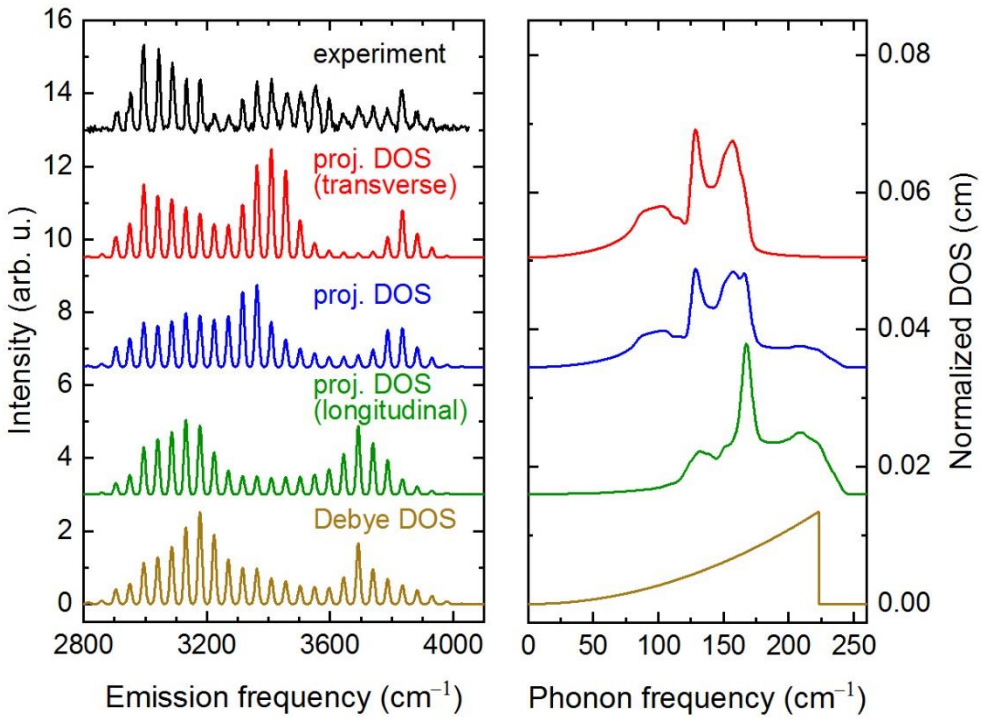

Figure 3 | Selective excitation of NaCl transverse phonons during energy pooling: The experimental emission spectrum (black solid line) is compared to kMC simulations assuming various NaCl phonon density of states spectra. In each simulation, the CO – to – CO interaction distance extends up to 34 Å. Each pooling step has an energy release to phonons of the solid; the probability depends on the density of phonon states at that energy. Shown are the results for a Debye DOS (brown) and three DFT-based DOSs: projection of the bulk DOS for NaCl onto the motion of the Na ions in the (100) plane (blue), longitudinal contribution to the projected DOS (green), and transverse contribution to the projected DOS (red).

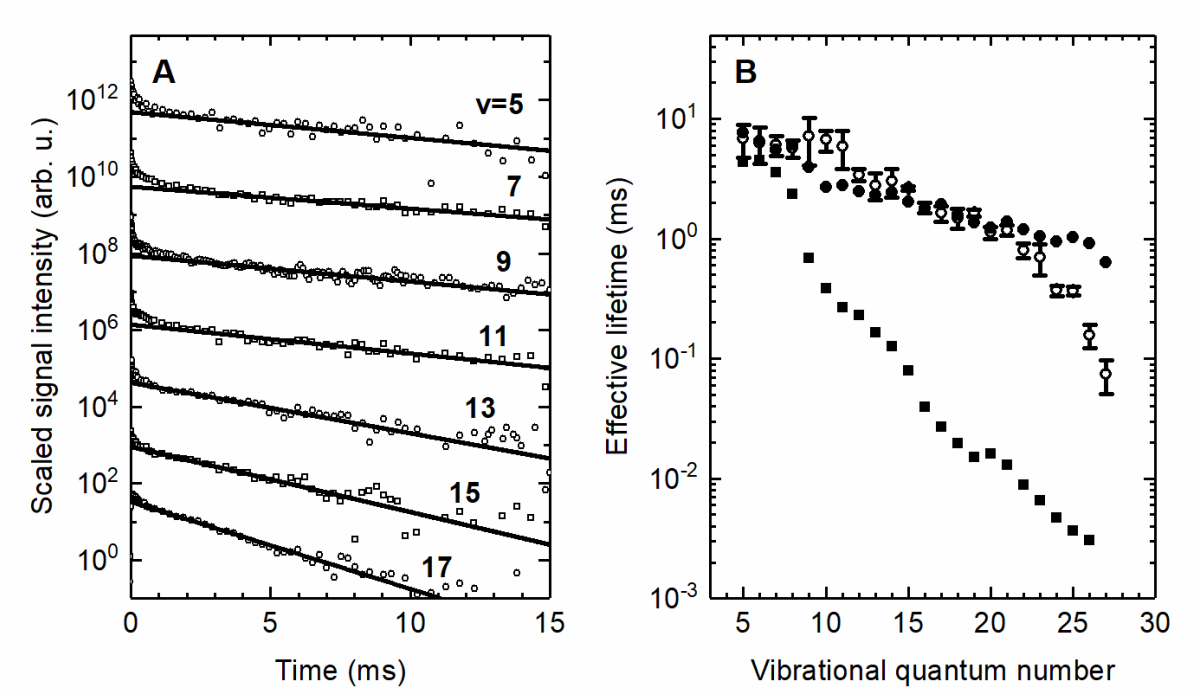

Figure 4 | Relaxation of CO to the NaCl solid follows the CPS model: Panel A shows representative temporal profiles of wavelength resolved infrared fluorescence (open symbols); the emitting vibrational state's quantum number is indicated. The long-time relaxation exhibits an exponential decay (black solid lines). Note the y-axis is logarithmic and that the data are offset from one another along the y-axis for clarity. The effective exponential lifetime obtained from these (and other) fits are shown in Panel B (black open circles with error bars). The kMC simulations also exhibit long-time exponential behaviour. The corresponding effective lifetimes are shown as solid symbols for two different vibrational relaxation models: the Skinner-Tully model (solid squares) and the CPS model (solid circles).

Supplementary Materials for

The Sommerfeld ground-wave limit for an adsorbed molecule at a surface

Li Chen, Jascha A. Lau, Dirk Schwarzer, Jörg Meyer, Varun B. Verma, Alec M. Wodtke

Correspondence to: alec.wodtke@mpibpc.mpg.de and li.chen@mpibpc.mpg.de

This PDF file includes:

Materials and Methods
Supplementary Text
Figs. S1 to S6

Materials and Methods

Experimental

The experimental apparatus has been described in detail (12, 13). Briefly, a monolayer of CO was prepared on a NaCl(100) surface by exposing the surface held at ≤ 55 K to isotopically purified $^{13}C^{18}O$ (Sigma-Aldrich, 99% atom ^{13}C and 99% atom ^{18}O) vapor. After the chamber had been evacuated, the sample was cooled to ~ 7 K with a closed-cycle liquid Helium refrigerator (RDK-408D2, Sumitomo). A narrow band infrared laser pulse (0.05 cm-1 FWHM bandwidth, 4.7 ns FWHM pulse duration, 10 Hz repetition rate and ~120 μJ pulse energy) was focused onto the surface to excite the adsorbed CO molecules via the fundamental C-O stretching vibration at 2055 cm^{-1}. The laser pumping of CO(v=0→v=1) transition is saturated, and a majority of the CO(v=0) molecules are vibrationally excited to the v=1 state. Laser-induced infrared fluorescence was dispersed through a home built liquid-nitrogen cooled grating monochromator. The wavelength-resolved temporal profiles were detected using a single photon counting detector based on an amorphous tungsten silicide (a-WSi) superconducting nanowire, whose output was recorded by a multichannel scaler (MCS6A-2, FAST ComTec GmbH).

Kinetic Monte Carlo Simulations

A rejection-free kinetic Monte Carlo algorithm based on the original FORTRAN code of Ref.'s (14, 17) was used. The code has been extended to include vibrational energy pooling beyond next-neighbor distances, overtone fluorescence, V-E transfer and stimulated emission. The simulation results are averaged over 50 trajectories where one trajectory consists of a 100×100 grid of $^{13}C^{18}O$ molecules in a square lattice (3.96 Å) with periodic boundary conditions. The simulation temperature of 11 K is chosen slightly above the experimental temperature of 7 K, which is measured next to the NaCl crystal. Initially all population is assumed to be in v=0 and we let the simulation evolve for about 33 ms after laser excitation. The highest vibrational state considered is v=35. Rate constants are calculated a priori for the following kinetic elementary steps (see section F of supplementary text for the corresponding equations): stimulated emission and absorption of the v=1←0 transition, vibrational energy pooling reactions, radiative and non-radiative vibrational relaxation processes, and V-E transfer for high vibrational states.

The laser excitation rate is simulated by a temporal Gaussian profile with a FWHM of 4.7 ns and a peak excitation rate of 3.44×10^{9} s^{-1}. The vibrational energy pooling rate constants for the reaction CO(n) + CO(m) → CO(n+1) + CO(m-1) are calculated based on the model presented in Ref.'s (14, 17). Since the dipole-dipole interaction potential between the CO molecules changes only slightly for the tilted (2×1) structure, we assume molecules oriented along the surface normal for convenience. The maximum interaction distance is about 34 Å unless otherwise stated. The integrals over the phononic DOS are calculated numerically considering energy pooling processes involving up to 3 phonons. Since the model assumes that the adsorbed CO molecules follow the surface-parallel motion of the Na ions underneath, a more realistic DOS is used by projecting the bulk DOS for NaCl onto the motion of the Na ions in the (100) plane. Radiative relaxation by fluorescence is treated as in Ref.'s (14, 16) including fundamental, 1st and 2nd overtone emission. Vibrational relaxation is based on the CPS model for all simulations except for the one shown in Fig. 4 (solid squares). Vibrational relaxation according to the Skinner-Tully model is based on Ref.'s (14-18), without further modifications, i.e., assuming a phonon DOS based on the Debye model coupled with the deformation potential approximation. V-E transfer is included for vibrational states with v≥28 using a fixed rate of 1×10^{5} s^{-1}, effectively transferring these vibrational states into v=0.

Supplementary Text

A. Preparation of monolayer and multilayer CO samples on NaCl(100)

The monolayer and multilayer CO samples are prepared by exposing the UHV-cleaved NaCl(100) surface to a backfilling CO pressure at controlled surface temperatures. Before gas admission, the surface is cleaned by briefly annealing to 390 K to remove any adsorbates (H_2, H_2O, CO and CO_2) (*32*), and the CO gas sample (Sigma-Aldrich, 99% atom ^{13}C and 99% atom ^{18}O) from a lecture bottle is purified using a liquid nitrogen trap. For preparation of a monolayer sample, the surface temperature is held at T_s= 55 K and a leak valve admits CO into the UHV chamber at a pressure of 1×10^{-6} mbar. This is continued until coverage is saturated; i.e., the FTIR absorption band remains unchanged with a further exposure. Next, we turn off the surface heating while slowly closing the leak valve and stop gas admission completely when the surface reaches T_s =35 K. We then hold the surface temperature at 35 K until the chamber pressure is below 5×10^{-10} mbar; this prevents growth of CO overlayers, which is possible only at T_s < 32 K (*30, 31*). Subsequently, the surface is cooled to the temperature needed for the experiment; typically 7 K. A multilayer sample is grown epitaxially on top of the monolayer (*30*) by additional CO dosing at T_s < 15 K. At a CO background pressure of 1×10^{-6} mbar, we observe a growth rate of about 100-monolayer per minute. After the dosing, the surface is briefly annealed to 25 K for several minutes to help form an equilibrium crystal structure of the multilayer sample (*31*).

B. $LiIO_3$ optical parametric amplifier laser

A tunable dye laser pulse at around 863 nm (LDS867 in ethanol, ~14 mJ, Cobra-Stretch, Sirah Lasertechnik GmbH) and a seeded 1064 nm laser pulse (130 mJ, 10 Hz, ca. 6 ns pulse width, Continuum Surelite III-10EX) are mixed in a temperature stabilized $LiIO_3$ crystal (100 ˚C) for difference-frequency generation (DFG). The dye laser is pumped by the 532 nm second harmonic output of the Nd:YAG laser. The DFG output is tuneable from 1950 to 2650 cm^{-1} with pulse energies in the range 70 μJ to 250 μJ.

The IR laser frequency is calibrated with photoacoustic spectroscopy of CO in a gas cell (ca. 10 mbar). Also from photoacoustic measurements, the bandwidth of the IR laser was determined to be 0.05 cm^{-1}. The pulse duration measured using the SNSPD was 4.7 ns (FWHM) (*13*).

C. Vibrational spectroscopic constants of CO/NaCl(100)

Based on an anharmonic oscillator model of the monolayer CO vibrational energy levels

$$E_{\mathrm{v}} = (\mathrm{v} + 1/2)\,\omega_e - (\mathrm{v} + 1/2)^2\,\omega_e x_e + (\mathrm{v} + 1/2)^3\,\omega_e y_e \qquad (1)$$

we assign the emission spectrum by fitting the measured overtone emission frequencies (S1) to the following expression:

$$\tilde{\nu}_{\mathrm{v}\to\mathrm{v}-2} = E_{\mathrm{v}} - E_{\mathrm{v}-2} = 2\omega_e - (4\mathrm{v} - 2)\,\omega_e x_e + 6\mathrm{v}(\mathrm{v} - 1)\,\omega_e y_e + \frac{7\,\omega_e y_e}{2}. \qquad (2)$$

This yields the spectroscopic constants ω_e = (2074.6 ± 0.9) cm^{-1}, $\omega_e x_e$ = (12.22 ± 0.04) cm^{-1} and $\omega_e y_e$ = (0.012 ± 0.002) cm^{-1}. The uncertainties result from 10 measurements on different days and different NaCl(100) sample surfaces. We note that the wavelengths identified by Eq. 2 differ from both CO gas phase and multilayer emission frequencies.

D. Vibrational state-resolved temporal profiles of CO overtone emission

The fluorescence intensity temporal profiles were measured using the SNSPD (*12*) together with a multi-channel scaler (MCS6A-2, FAST ComTec GmbH). We determined the time zero by measuring the arrival time of scattered laser light. The monochromator was tuned to each of the detected overtone (v→v-2) emission lines (main manuscript, Fig. 2). All temporal profiles were recorded in a time range of –1.0 to 50 ms with a bin-time of 51.2 ns in order to follow the rapid vibrational energy pooling dynamics as well as the slow relaxation dynamics. The measured raw data were re-binned to achieve satisfactory S/N ratio at a cost of reduced time resolution. The acquisition time varied between 6 and 26 minutes depending on the signal intensity.

Fig. S2 presents fluorescence temporal profiles for all the monolayer CO vibrational states (v=4-27) detected in this experiment on a linear (Fig. S2-A) and logarithmic time-scale (Fig. S2-B). The fluorescence rise is faster than 1 μs for the lower states v=4-12 and cannot be resolved due to insufficient S/N.

E. Calibration of *absolute* vibrational populations

We convert the measured dispersed fluorescence intensity temporal profiles $I_n(t)$ to relative time-dependent populations $P_n(t)$ for each vibrational state n as was described in Ref. (*12*):

$$P_n(\mathrm{t}) = \frac{I_n(\mathrm{t})}{\eta \cdot k_\mathrm{f}}. \tag{3}$$

η and k_f are the wavelength dependent system detection efficiency and the fluorescence rate, respectively. Fig. S3 shows the relative error of $P_n(\mathrm{t})$ derived from fluorescence spectra integrated over 0.05-1.05 ms.

We estimate the absolute population by comparison with the kinetic Monte Carlo (kMC) simulation. At short times after the laser pulse, the total number of vibrational quanta in the CO monolayer is conserved because vibrational energy loss is unimportant. In other words, $\sum_n n \cdot P_n(t) \approx const.$ for $t < 10$ μs. From our kMC simulation, $\sum_n n \cdot P_n(t = 1\ \mu\mathrm{s}) = 0.73$ was determined and used to calculate the absolute time-dependent vibrational populations in Fig. S2.

F. Rate constants for kinetic Monte Carlo (kMC) simulations

Vibrational dynamics in the CO monolayer on NaCl is governed by the interplay of vibrational energy pooling (VEP), fluorescence, non-radiative CO vibrational energy transfer to the NaCl substrate and vibration-to-electronic (V-E) energy transfer. We calculate the corresponding rate constants based on available theoretical models. The results are summarized in Fig. S4.

1. Fluorescence rate constants

The fluorescence rate constants, k_f, are calculated based on standard spectroscopic relationships (*12, 14, 16*) using the following parameter values for the monolayer $^{13}C^{18}O$ on NaCl (100): slope of the electric dipole moment function μ'= 3.2 D/Å (assuming the optical and physical properties of the physisorbed CO on NaCl do not change appreciably from those of the gas-phase)

(*33*), Morse parameter a = 2.34 Å^{-1}, and the spectroscopic constants ω_e= 2074.6 cm^{-1} and $\omega_e x_e$ = 12.22 cm^{-1} (see Section C). Note that the calculated rates for 1st overtone (Δv=2) and 2nd overtone emission (Δv=3) are also included in the kMC simulations but not shown in Fig. S4.

2. Vibrational energy pooling rate constants

The VEP rate constants are calculated based on the model from Corcelli and Tully (*14, 15, 17*) with a modified treatment of the NaCl phonon spectrum. Note that there is a minor typographical error in the formula for $k_{nm}^{(p)}$ in Ref. (*14*) but Corcelli's PhD thesis (*17*) shows the correct equation. The pooling rate constant, k_{nm}, for a pooling reaction CO(n) + CO(m) → CO(n+1) + CO (m-1) for a given distance R (in SI units) is:

$$k_{nm} = \sum_{p=1}^{p_{\max}} k_{nm}^{(p)} \tag{4}$$

$$k_{nm}^{(p)} = \frac{2\pi}{\hbar} p!\, f_p^2 2^p |\langle n|x|n+1\rangle|^2 |\langle m|x|m-1\rangle|^2 \left(\frac{(n(E_{nm}/p)+1)\hbar}{2M}\right)^p I_p \tag{5}$$

$$f_p = (-1)^p \frac{\mu'^2 (p+1)(p+2)}{(4\pi\varepsilon_0) 2R^{p+3}} \tag{6}$$

$$I_p = \int_0^\infty \mathrm{d}E_1 \cdots \int_0^\infty \mathrm{d}E_p \frac{\rho(E_1)}{E_1} \cdots \frac{\rho(E_p)}{E_p} \delta(E_{nm} - E_1 - \cdots - E_p) \tag{7}$$

$$n(E) = \left(\exp\left(\frac{E}{k_B T}\right) - 1\right)^{-1} \tag{8}$$

where p is the number of phonons involved and $p_{\max} = 3$, since processes involving more than 3 phonons do not yield significant rate constants for all n-m transitions that are of relevance here (*14*). M is the mass of a Na atom (23 amu). The matrix elements of the relative bond coordinate x are calculated as for the fluorescence rate constants (see Ref.'s (*12, 14, 16, 33*)). The electric dipole moment function is assumed to be linear with a slope of $\mu' = 3.2$ D/Å, for the same reason as in the calculation for the fluorescence rate constants. The integrals I_p are evaluated numerically for a given phonon density of states (DOS), $\rho(E)$, which is normalized such that $\int_0^\infty \mathrm{d}E\, \rho(E) = 1$, where the energy mismatch E_{nm} is positive for exothermic reactions. Rate constants for reverse endothermic reactions are derived from the rate constants of the exothermic reactions by detailed balance.

Phonons for bulk NaCl in the rock-salt structure are calculated based on density functional theory (DFT) using the exchange-correlation functional due to Perdew, Burke and Ernzerhof (*34*) as implemented in the FHI-aims all electron DFT package (*35*). Tight settings are used for the basis sets and integration grids together with equivalents of a 4×4×4 Monkhorst-Pack grid (*36*) for the Brillouin zone sampling in the primitive unit cell. These settings yield a perfectly converged lattice constant of 5.698 Å in excellent agreement with earlier all-electron DFT calculations (*37-39*) and a well-converged phonon DOS.

Force constants are calculated according to the finite displacement method (*40*) in 4x4x4 supercells of the primitive unit cell with optimal exploitation of symmetry as implemented in the phonopy code (*41*). The total phonon DOS is then obtained based on a Fourier-interpolated 40×40×40 grid of phonon-wave vectors **q** for all six phonon bands *i*, where $E_{\mathbf{q}i}$ is the corresponding energy equivalent of each phonon:

$$\rho^{\text{total}}(E) = \frac{1}{6}\sum_{\mathbf{q}}\sum_{i=1}^{6}\delta\left(E - E_{\mathbf{q}i}\right) \tag{9}$$

Here and in the following, the delta functions are broadened by Gaussians with a very small width of only 2.42 cm^{-1} thanks to very dense **q**-grid. Fig. S5 shows the results of the phonon DOS calculations used in this work.

The model by Corcelli and Tully is based on the modulation of the dipole-dipole interaction between two CO molecules. This is caused by phonons in the NaCl surface, that change the lateral distance between two COs. These are phonons that involve lateral movement of the Na atom directly beneath each CO molecule (see Fig. S6). Consequently, we use a phonon DOS that is projected onto phonons which include Na-atom displacements in the (100) plane. Furthermore, using the scalar product between the atom-wise displacement and the wave vectors of each phonon, we construct the projected phonon DOS for transverse (T) or longitudinal (L) phonons

$$\rho^{\text{Na,(100); T,L}}(E) = \frac{1}{3}\sum_{\mathbf{q}}\sum_{i=1}^{6}\delta\left(E - E_{\mathbf{q}i}\right)\left|\mathbf{p}_{\mathbf{q}i}^{\text{Na;T,L}}\right|^2. \tag{10}$$

$\mathbf{p}_{\mathbf{q}i}^{\text{Na;T,L}}$ is the transverse or longitudinal contribution of the normalized displacement vector $\mathbf{e}_{\mathbf{q}i} = \left(\mathbf{e}_{\mathbf{q}i}^{\mathbf{Na}}, \mathbf{e}_{\mathbf{q}i}^{\mathbf{Cl}}\right)$ for Na atoms only, i.e., entries for $\mathbf{e}_{\mathbf{q}i}^{\mathbf{Cl}}$ are set to zero:

$$\mathbf{p}_{\mathbf{q}i}^{\text{Na;T}} = \left(\frac{\mathbf{q}\cdot\mathbf{e}_{\mathbf{q}i}^{\mathbf{Na}}}{|\mathbf{q}|}\frac{\mathbf{q}}{|\mathbf{q}|}, 0\right) \tag{11}$$

$$\mathbf{p}_{\mathbf{q}i}^{\text{Na;L}} = \left(\mathbf{e}_{\mathbf{q}i}^{\mathbf{Na}} - \frac{\mathbf{q}\cdot\mathbf{e}_{\mathbf{q}i}^{\mathbf{Na}}}{|\mathbf{q}|}\frac{\mathbf{q}}{|\mathbf{q}|}, 0\right). \tag{12}$$

Unless otherwise stated, all simulations are based on the transverse, projected DOS, which yields excellent agreement with experiment. See Fig. 3 in the main text.

Rate constants for resonant energy V-V exchange are also calculated according to Ref.'s (*14*, *17*):

$$k_{n,n+1} = \frac{\mu'^2\langle n|x|n+1\rangle^2}{\hbar\cdot\arccos(e^{-1/2})(4\pi\varepsilon_0)R^3}. \tag{13}$$

For two nearest neighbor CO molecules, the non-resonant rate constants k_{n1} are on the order of 10^7 to 10^8 s^{-1}. The resonant rate constants are much larger, e.g. $k_{01} = 1.8\times10^{11}$ s^{-1}. The high resonant rate constants allow for fast diffusion of single vibrational states but significantly slow down the kMC simulations. To reduce the computation time, the resonant rate constants are scaled by a factor of 1/100. No notable change in the vibrational energy distribution was found in test simulations with a scaling factor of 1/10.

3. The Skinner-Tully model of CO vibrational energy transfer to the NaCl substrate

Fig. S6A depicts the ST model used for describing CO vibrational energy transfer to the NaCl substrate (*14, 15, 17, 18*).

In this model, we calculate the non-radiative CO-NaCl energy transfer rate constants for a given vibrational state n as (in SI units)

$$k_{\mathrm{nr}}^{\mathrm{ST}} = \sum_{p=1}^{p_{\max}} k_n^{(p)} \tag{14}$$

$$k_n^{(p)} = \frac{1}{\hbar}|\langle n|x|n-1\rangle|^2 \left[n\left(\frac{E_n}{p}\right)+1\right]^p \frac{f_p^2 I_p}{E_n p!} \tag{15}$$

$$f_p = (-1)^p(2^{p+1}-2)D'\alpha'^{p+1}a_o^p \frac{m_{\mathrm{O}}}{M_{\mathrm{CO}}} \tag{16}$$

$$I_p = \lambda^p \frac{E_n}{hc\tilde{\nu}_{\mathrm{D}}}\sqrt{\frac{75\pi}{p}}\exp\left[-\frac{75}{4p}\cdot\left(\frac{E_n}{hc\tilde{\nu}_{\mathrm{D}}}-\frac{4p}{5}\right)^2\right] \tag{17}$$

where E_n is the energy dissipated to phonons. The sum in Eq. 14 is truncated at $p_{\max} = \mathrm{int}(E_n/\omega_D) + 11$, since processes involving more phonons do not yield any further significant contributions. m_{O} and m_{CO} are the masses of ^{18}O and ^{13}C^{18}O, respectively, $D' = 10.917$ eV and $\alpha' = 2.34$ Å^{-1} are the parameters of the Morse-type CO-NaCl adsorption potential, a_0 is the Bohr radius, $\lambda = 0.522$ an empirical parameter describing the global system-bath coupling, and $\tilde{\nu}_{\mathrm{D}} = 223$ cm^{-1} the Debye frequency of NaCl in cm^{-1} (*14*). Other quantities are the same as in Section F.1 and F.2. Note that the original work by Corcelli and Tully contains two typographical errors in the formula for I_p. The corrected equations from Ref. (*16*) are used, where we would like to point out another small typographical error in the formula for $k_n^{(p)}$.

The ST model predicts a strong vibrational state dependence (v-dependence) of k_{nr} as shown in Fig. S4. The rate constants increase by more than five orders of magnitude between v=1 and v=25. Note that the Skinner-Tully model relies on a coupling strength parameter, λ, which was deduced empirically by matching the total fluorescence decay time constant (τ =4.3 ms) reported by Chang and Ewing (*11*) to kMC simulations in Ref. (*14*). According to Eq. 14-17, the absolute magnitude of $k_{\mathrm{nr}}^{\mathrm{ST}}$ is extremely sensitive to λ. However, we found that the dependence on λ is quite similar for all the v states; hence, we expect that the strong v-dependence of $k_{\mathrm{nr}}^{\mathrm{ST}}$ shown in Fig. S4 remains at all values of λ. Note also that adjusting the Debye frequency in Eq. 17 has a similar effect.

4. The Chance-Prock-Silbey model of CO vibrational energy transfer to the NaCl substrate

The CPS model (Fig. 6B) differs markedly from the ST model and has been described in detail in several seminal papers (*19, 20, 42, 43*). In particular, we recommend the review of Ref. (*19*). CPS is based on electromagnetic coupling to the solid, which absorbs and reflects light at the CO transition frequency, while the ST model relies on anharmonic coupling via the CO-NaCl surface bond. CPS was originally developed to explain the experimentally observed changes in fluorescence lifetime of an electronically excited molecule as its distance from a metallic surface is varied (*24, 26, 29*). Experimental control of the distance was accomplished by the introduction of inert organic spacer layers in the form of Langmuir-Blodgett-Kuhn films (*44*). Kuhn initially described the variation of lifetime with distance as a dipole emitter interacting with its electromagnetic echo field – i.e. the field reflected from the mirror. In his view, lifetime change is essentially a retardation effect where interference occurs between the emitting dipole and the image dipole set up in the solid. CPS showed that additional effects become important when the molecule comes close to the mirror, specifically creation of dipole-carrying excitations (e.g. plasmons and optical phonons) that are linked to the imaginary part of the solid's refractive index, κ. Working with a mathematical formalism written down to describe radio transmission in the presence of a partially conducting Earth (*45*), one that had its origins in Sommerfeld's ground wave paper (*21*), CPS were able to derive an exact expression within the classical limit that was valid at all distances (*20*) and gave excellent agreement with experiment (*43*).The most important extension in the theoretical treatment of CPS was to separate the lifetime of the dipole emitter into a radiative component, essentially the fluorescence lifetime, and a non-radiative component, where energy is transferred to the solid.

In the limit of small distances ($d \to 0$), the CPS model provides an analytic solution for the non-radiative energy transfer rate to the solid. The rate constant, $k_{\mathrm{nr}}^{\mathrm{CPS}}$, is directly proportional to the square of the transition dipole moment of the molecule, which is proportional to $k_{\mathrm{f}}/\tilde{\nu}^3$, as well as the imaginary part of the index of refraction, κ (*19, 46*).

$$\frac{k_{\mathrm{nr}}^{\mathrm{CPS}}}{k_{\mathrm{f}}} = \frac{3\theta n\kappa}{16\pi^3\tilde{\nu}^3|\epsilon+1|^2 d^3}. \tag{18}$$

where $\tilde{\nu}$ is the CO emission frequency in cm^{-1}, $\epsilon = (n + \mathrm{i}\,\kappa)^2$ is the frequency dependent complex dielectric constant of NaCl at the emission frequency, θ is the orientation parameter and is 1 for perpendicular dipole orientation, and d is the molecule's distance from the surface. For CO on NaCl: $d = R_{\mathrm{C-Na}} + M_{\mathrm{O}}/(M_{\mathrm{O}} + M_{\mathrm{C}})\, R_{\mathrm{C-O}} = 3.36$ Å and is the distance of the CO center-of-mass to the NaCl interface, where $R_{\mathrm{C-Na}} = 2.7$ Å and $R_{\mathrm{C-O}} = 1.14$ Å (*47*). M_{O} and M_{C} are the masses of ^{18}O and ^{13}C, respectively. The refractive index n and the extinction coefficient, κ, are almost constant (n = 1.52 and $\kappa = 1.8\times10^{-9}$) in the mid-IR wavelength range relevant to our work (1500-2600 cm^{-1}) (*48*). While κ is quite small – NaCl is nominally transparent in the mid-infrared, this value is still large enough to have a clearly observable effect. We then calculate the v-dependent rate constants using the calculated CO gas phase fluorescence rates k_{f}(v) shown in Fig. S4 and the fundamental emission frequencies $\tilde{\nu}(\Delta \mathrm{v} = 1)$ of the monolayer ^{13}C^{18}O determined from Eq. 1.

The calculated values for $k_{\mathrm{nr}}^{\mathrm{CPS}}$ in Fig. S4 show a much weaker v-dependence than $k_{\mathrm{nr}}^{\mathrm{ST}}$, which is closely related to the v-dependence of the radiative rate constants k_{f}. This is a qualitative characteristic of the CPS model reflecting coupling via the electromagnetic field. This aspect of the CPS improves our confidence that even a more sophisticated treatment of the ST model or

another model based on mechanical coupling via the anharmonic potential energy surface would fail to agree with our experimental observations (Fig. 4B Main text). The ratio $k_{\mathrm{nr}}^{\mathrm{CPS}}/\,k_{\mathrm{f}}$ changes from 5 (v=1) to 13 (v=27) due to the $\tilde{\nu}^{-3}$ dependence of Einstein A-coefficients, k_{f}, appearing in Eq. 18. The CPS model also predicts a reduction of the fluorescence rate by 10% due to interference of the emitted photon with itself upon reflection from the surface. Since k_{f} is about one order of magnitude smaller than $k_{\mathrm{nr}}^{\mathrm{CPS}}$, this effect on the emission rate is neglected in our simulations.

5. Vibrational-to-electronic (V-E) energy transfer rate constants

In our experiment, we do not observe any population in v=28 or higher. The vibrational energy of CO (X $^1\sum^+$, v=28) is 6.01 eV, in close resonance with the vibrational ground state of the first electronic excited state (6.01 eV) of CO molecules in the gas phase. Thus, we assume a V-E energy loss channel in the kMC simulation. We set the corresponding rate constants to 1×10^5 s^{-1} for vibrationally excited states above v=27, which avoids accumulation of population in these states.

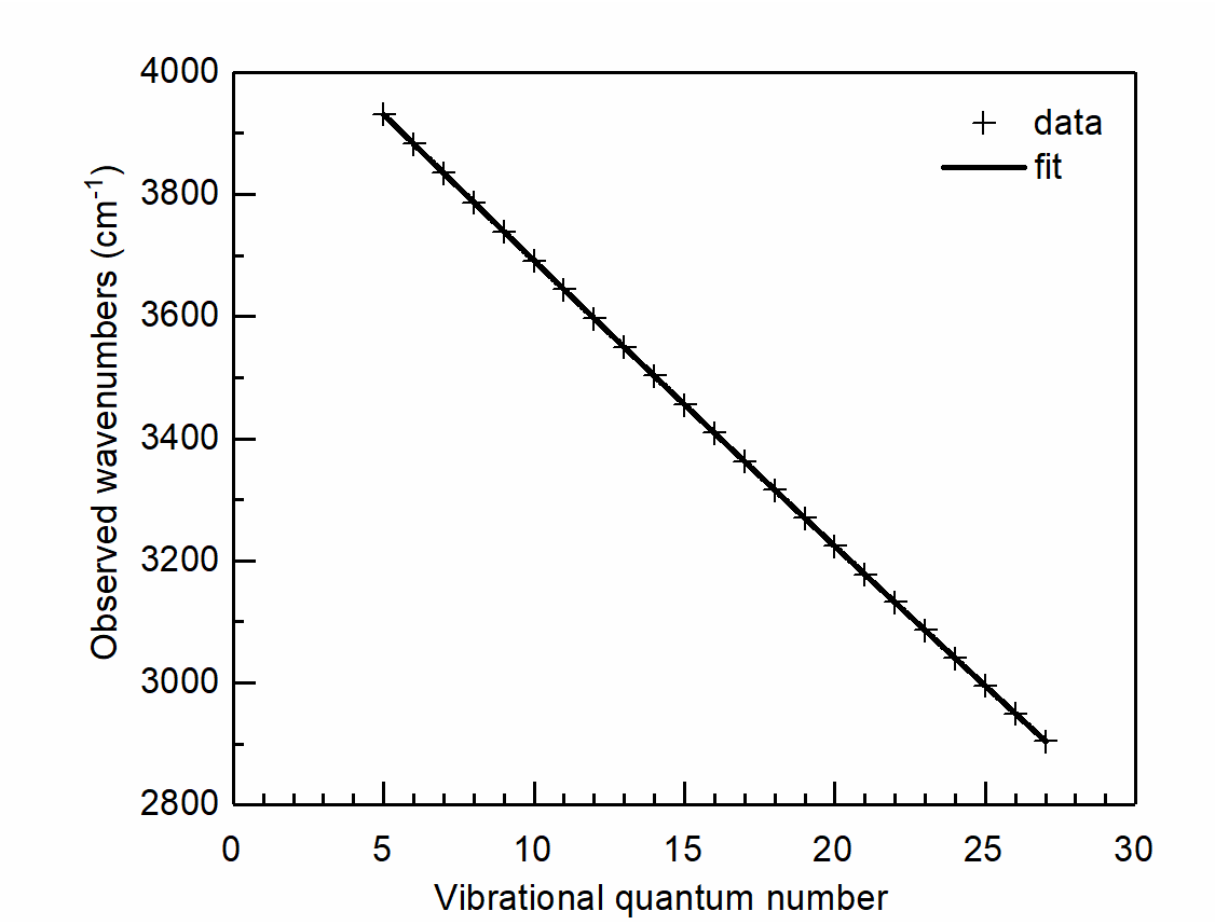

Figure S1 Observed wavenumbers for CO overtone emissions (v→v-2) from a monolayer $^{13}C^{18}O$ on NaCl (100), see Fig. 2 in the main manuscript. The solid line is a least-square fit to the data based on Eq. 2.

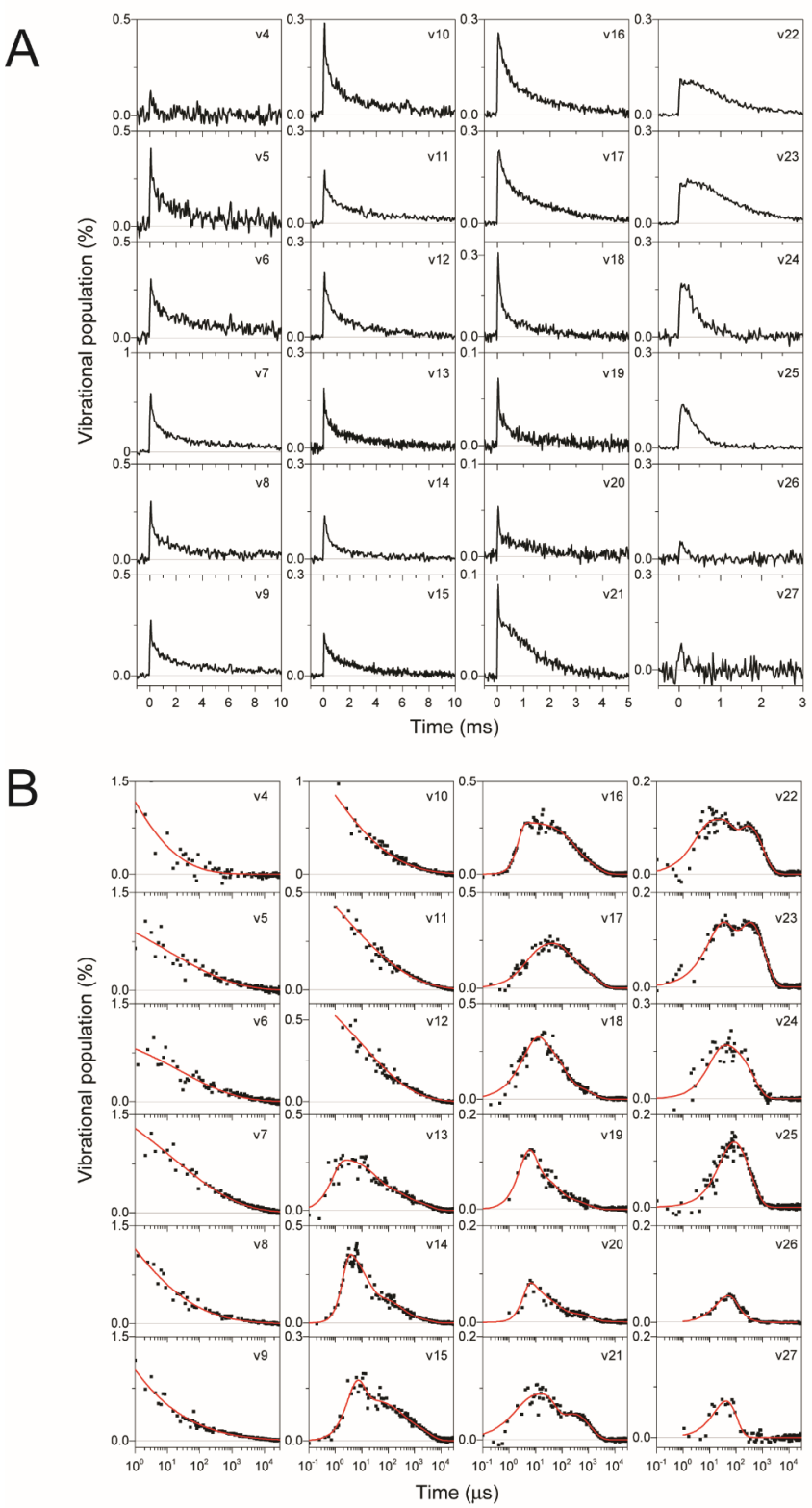

Figure S2 │Temporal profiles of the CO monolayer overtone emission for the vibrational states 4-27 at 7 K. Panel A and B show the temporal profiles on a linear and logarithmic time-scale, respectively. Note the different time ranges for different vibrational states. The vibrational population shown on the y-axis is calibrated according to Section E. Panel A: Temporal profiles are shown with a bin-time of 25 µs. Panel B: The bin-time increases with time. Red lines are empirical fits to the experimental data to guide the eye.

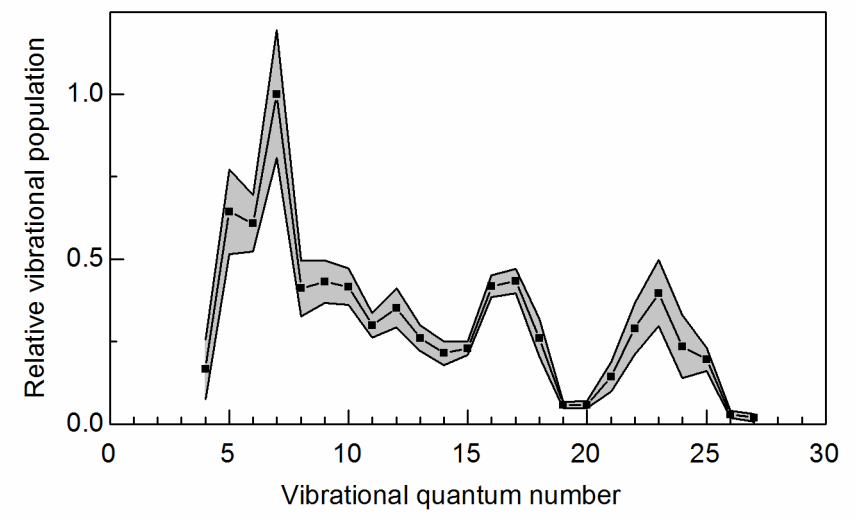

Figure S3 │The relative vibrational population distribution of monolayer CO integrated over 0.05-1.05 ms (black dots). The grey shaded region represents the overall uncertainty.

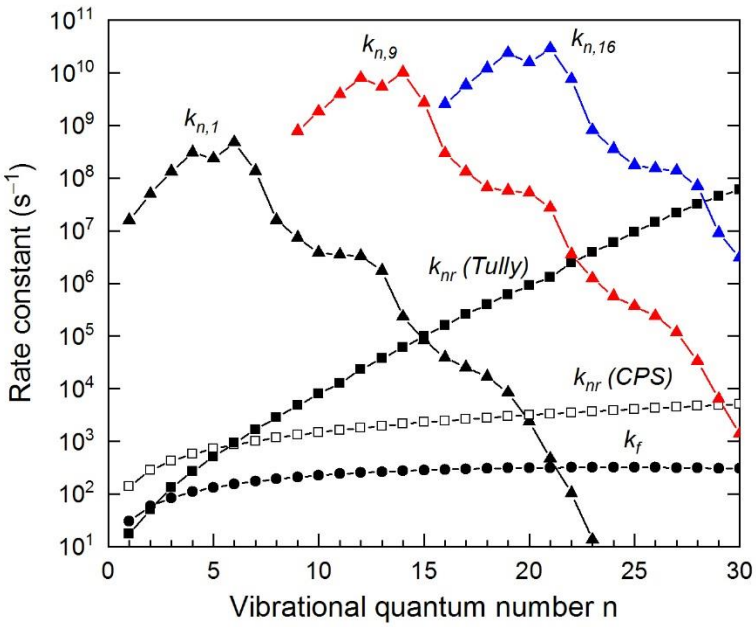

Figure S4 │ Rate constants calculated for the kMC simulations. Shown are rate constants for single-quanta processes: fluorescence (filled circles), nearest neighbor vibrational energy pooling CO(n) + CO(m) → CO(n+1) + CO (m-1) for selected states m=1, 9 and 16 (triangles), and non-radiative relaxation for the Tully (filled squares) and the CPS model (open squares). Note that the VEP rate constants depend strongly on distance (see Section F.2 for details).

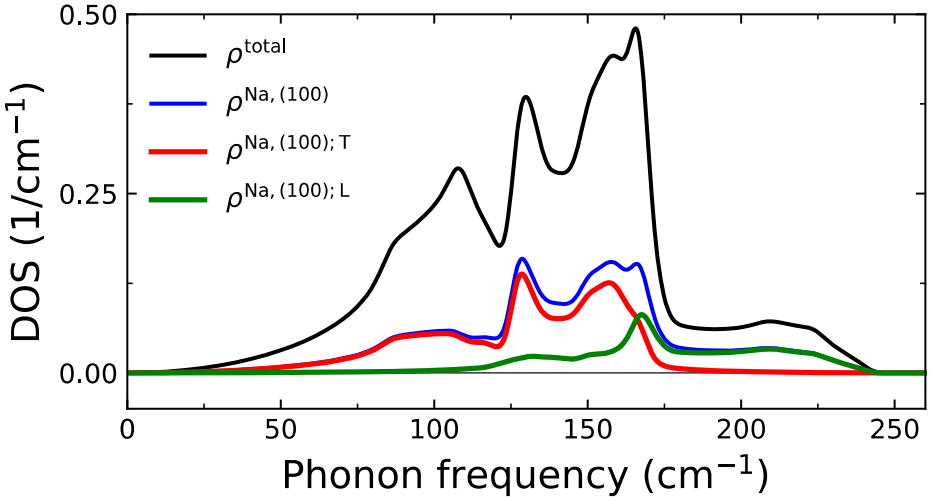

Figure S5 | Phonon density of states (DOS) for bulk NaCl. Shown are the total DOS (black solid line), the DOS projected onto phonons which include Na-atom displacements in the (100) plane (blue) together with its decomposition into transverse (T, red) and longitudinal (L, green) phonons as defined by Eq. 10-12 in the text. The DOSs are plotted as a function of phonon frequencies corresponding to the phonon excitation energies *E*. The total DOS is normalized to 1, and the transverse and longitudinal projections sum up to to the Na-atom-(100) projection.

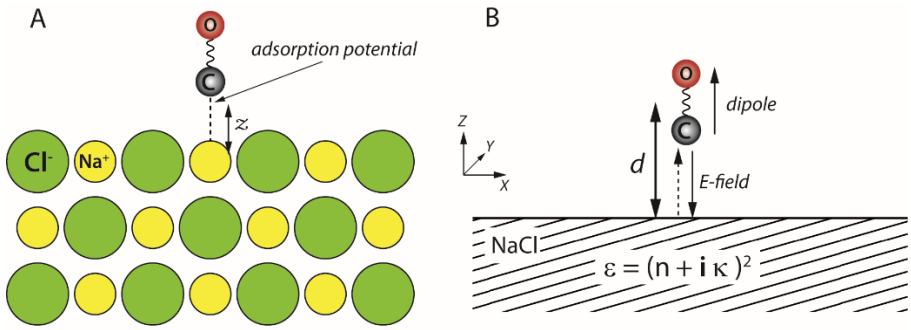

Figure S6 │ Theoretical models for describing vibrational energy transfer of adsorbed CO molecules to the solid NaCl substrate. (A) Tully model: Vibrational energy flows by mechanical coupling of the CO oscillator to the bulk NaCl phonon bath by anharmonic interaction through the C-Na^+ bond. (B) CPS model: Vibrational energy flows from the molecule to the solid via the electromagnetic field emitted by the oscillating CO dipole near the NaCl half-space with a complex frequency dependent dielectric constant. Note that the CPS model is not defined in terms of atoms and forces between them.